CrossMark

Unveiling Ultra-High Temperature Wear and Indentation Damage Mechanisms of Thermal Barrier Coatings

CLIFTON BUMGARDNER[1] and XIAODONG LI[1,2]

1.—Department of Mechanical and Aerospace Engineering, University of Virginia, 122 Engineer's Way, Charlottesville, VA 22904, USA. 2.—e-mail: xl3p@virginia.edu

Thermal barrier coatings are necessary to protect turbine blades within jet engines from extreme environments that the substrate material may not be capable of withstanding. Therefore, failure of the coating due to wear during its operational lifecycle is a critical event. In order to understand the failure mechanisms of the coating layers, a zirconia-based coating on a nickel alloy substrate was subjected to wear testing to simulate pressure and temperature conditions within a jet engine. Using a Hertzian contact model, the maximum shear and its depth were determined and analyzed in conjunction with the coating material properties and scanning electron microscopy and energy dispersive x-ray spectrometry images. The coupled imaging and contact model analyses made possible the identification of the location and time of delamination and its underlying causes. Our findings provide key insights for the development of more resilient thermal barrier coatings.

INTRODUCTION

Thermal barrier coatings (TBCs) are frequently used, especially in the aviation industry, for thermal and wear protection. Jet engine turbine blades can be exposed to temperatures as high as 1300°C, and the force of superheated air passing through the turbine can generate pressures up to 3.5 MPa.[1,2] For many metals, the operating temperature of a turbine is beyond their melting points, requiring the coating to serve as a thermal barrier between the extreme heat. If the coating is unable to sustain the pressure, it may fail, break off, and expose the metal.[2] For this reason, turbine blade failure in a jet airliner, especially a passenger airliner, can have disastrous effects.

To prevent coating failure, it is necessary to establish a comprehensive understanding of the mechanisms that build up to it. In keeping with prior examinations of TBC wear mechanisms, this study used tribological testing to wear a sample of thermal barrier coating to simulate conditions within a jet engine to determine when failure occurred.[3,4] Furthermore, a control test was run at room temperature, 23°C, for a comparison analysis to evaluate the impact thermal expansion had on the mechanisms of failure. Microscopy imaging and energy dispersive x-ray spectrometry provided detailed images of wear damage and layer delamination as successfully demonstrated by previous research.[5,6]

This research builds upon substantial prior work by incorporating analysis of coating properties and failure behavior at temperatures of 1000°C to replicate the operating temperature for many applications of ceramic coatings. Previous studies have examined the effect of sliding contact, coating thickness, and friction coefficient on the stresses within TBCs.[7,8] Others have focused on particle impingement on TBCs to observe the impact on internal stresses and cracking.[9] Further research has targeted the residual stresses of yttria-stabilized zirconia using the curvature method and Raman spectroscopy after heat treatments to 1150°C.[10] Combining our experimental approach with insights from previous research on sliding contacts, layer material properties, and thermal stress, we can provide an in-depth understanding of the mechanisms and the principal contributing factors to coating failure. From this understanding, it may be possible to identify material properties of coating layers that require improvements to prevent or delay failure.
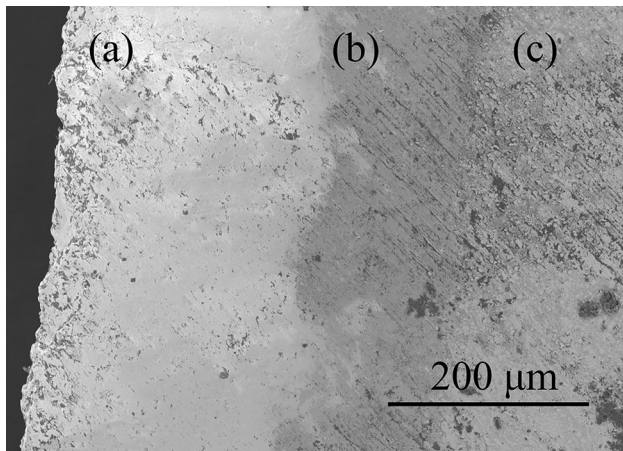
Fig. 1. A cross-sectional image of the thermal barrier coating showing the thickness of the layers: (a) 8YSZ top coat, (b) NiCoCrAlY bond coat, and (c) the Ni alloy substrate.

Fig. 2. Under a normal load of 1 N, the in situ COF is presented at ▶ 1000°C (a) and 23°C (b). Under a normal load of 2 N, in situ COF at 1000°C (c) and 23°C (d) is presented. Under a normal load of 3 N, the in situ COF at 1000°C (e) and 23°C (f) is presented. Under a normal load of 4 N, the in situ COF at 1000°C (g) and 23°C (h) is presented. Under a normal load of 5 N, the in situ COF is presented at 1000°C (i) and 23°C (j).

EXPERIMENTAL DETAILS

All wear and indentation tests were conducted on a specimen of a nickel-based superalloy, Haynes HR-224, composed of Ni-27.5Fe-20Cr-3.8Al.[11] This nickel alloy substrate was chosen as the substrate material due to its high temperature strength and oxidation resistance, factors determined by previous studies to be critical for operation within a turbine engine.[12,13] A thermal barrier coating of yttria-stabilized zirconia (8YSZ) and a bond coat of NiCoCrAlY were applied to the specimen using an air plasma spray deposition process, layered as shown in Fig. 1. Both coating materials were selected due to their wide use in industry and in research analysis.[3,6,10]

Wear and indentation analyses of the sample were conducted using a Bruker UMT-3 tribometer (Bruker Nano, Campbell, CA, USA), which was capable of measuring normal and lateral forces as well as the displacement of the indenter. All wear tests were conducted within a furnace chamber in air, either heated to a high temperature (1000°C) to best model the air intake of a turbine or to room temperature (23°C) as a baseline. Under applied loads ranging incrementally from 1 N to 5 N, the wear tests were run for 1 h each, 19,098 cycles at both room and high temperatures. During the tests, the tribometer collected measurements of normal (N) and lateral forces, frictional force (F_f), and used these measurements to calculate the coefficient of friction (COF), using the following equation: $F_f = COF \times N$.[14] A 6.3-mm-diameter alumina ball was used as the indenter for wear tests where the ball was oscillated with a frequency of 33.3 Hz.

Indentation tests were conducted with a sapphire Vickers indenter at both room and high temperatures. Indentations were made into a TBC cross-section sufficiently thick to prevent any influence from the mounting device and with indentations spaced 5 mm apart.

RESULTS AND DISCUSSION

Friction Analysis and Volume Loss During Wear

Figure 2a, c, e, g, and i plots the coefficient of friction over the hour-long tests for each applied load at 1000°C. Figure 2a and c displays a significant change or sudden jump in the coefficient of friction at some point during the test. This change or shift is due to the failure and delamination of one or more layers within the coating. The point of this jump occurs late in the test with an applied load of 1 N, but under an applied load of 2 N, the jump occurs over 15 min earlier. If such a trend continues at higher loads, the jump should occur within the first 8 min under a load of 3 N and almost instantly under higher normal loads.

Indeed, under an applied normal load of 3 N (Fig. 2e), there is a prolonged period of higher coefficient of friction before it gradually decreases and evens out after 6 min. In subsequent tests under normal loads of 4 N and 5 N (Fig. 2g and i, respectively), there is an initial peak within the first minute of testing and a quick transition into a steady state. This behavior supports the hypothesis that delamination has occurred at an increasing rate with the increasing normal load.

The same procedure was repeated for wear at room temperature (23°C). The coefficient of friction was calculated and plotted as shown in Fig. 2b, d, f, h, and j. With the exception of the test with an applied load of 1 N (Fig. 2b), there was a common trend among the room temperature wear tests: the friction coefficient and the force of friction would rise quickly as the test began, reaching a point where it leveled out. Unlike the tests at high temperature, there was no shift of significant change in the friction coefficient to indicate that delamination had occurred. Instead, the occasional variances in the COF plots can be attributed to surface wear at the interface with the indenter. Visual inspection of the wear tracks confirmed light wear at room temperature and more severe wear at high temperature.

Table I lists the recorded values of friction force and coefficient of friction taken at the start and end of testing. The initial values represent both the friction of the top coat and the impact of stiction, the necessary force required to overcome static friction and allow motion.[11] During the high-temperature testing, the initial frictional force increased with the applied normal load as expected, but this trend did

Coefficient of Friction

(a) COF at 1000 °C — Applied Normal Load: 1N

(b) COF at 23°C — 1N

(c) 2N COF at 1000 °C

(d) 2N COF at 23°C

(e) 3N COF at 1000 °C

(f) 3N COF at 23°C

(g) 4N COF at 1000 °C

(h) 4N COF at 23°C

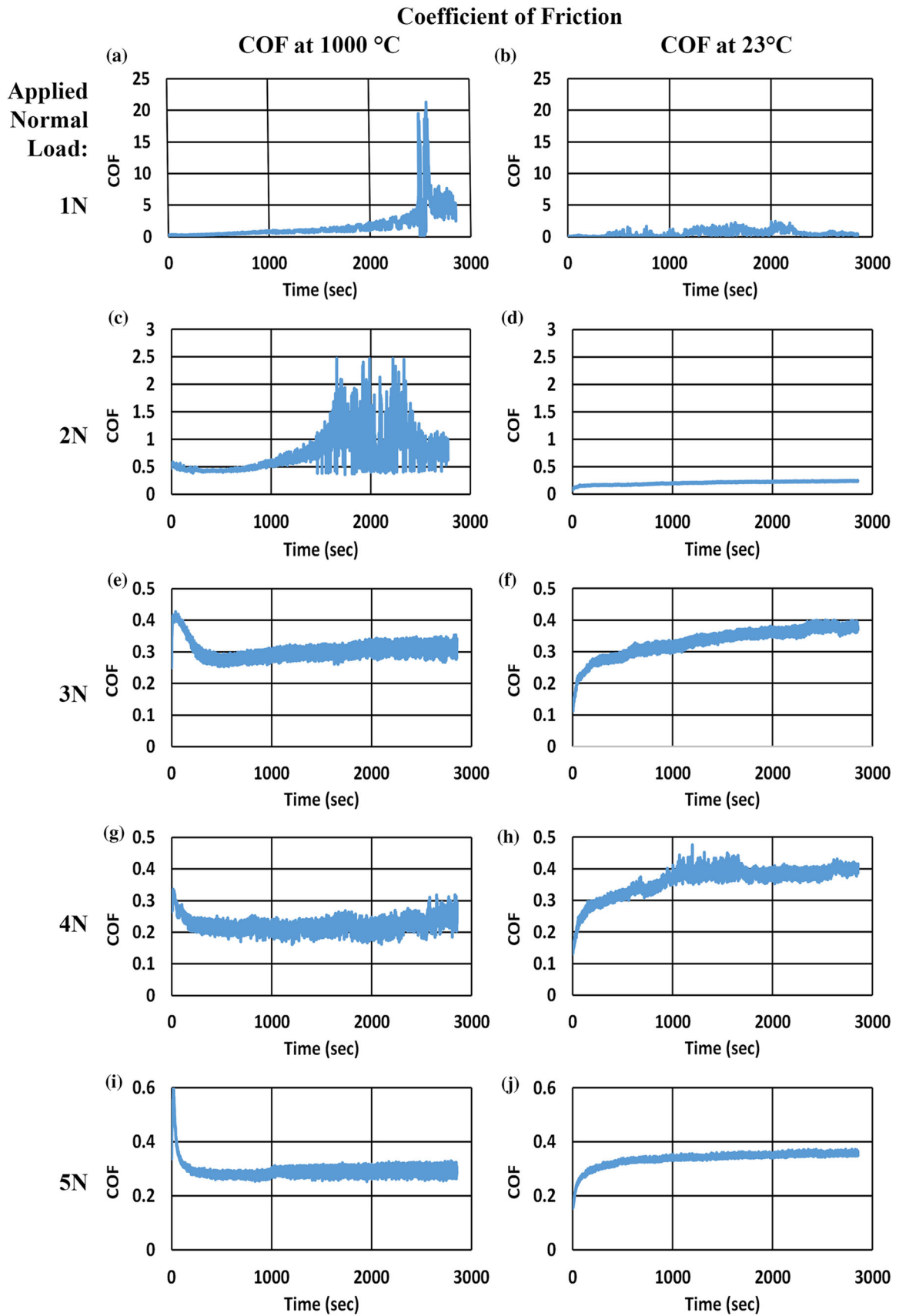(i) 5N COF at 1000 °C

(j) 5N COF at 23°C

Table I. Initial and final friction and coefficient of friction values, wear depth (calculated based on the change in the measured height of the indenter), and wear rate (calculated by wear depth, dimension of the indenter, and time)

			High temperature (1000°C) wear testing			
Normal force (N)	Initial F_f (N)	Initial COF	Final F_f (N)	Final COF	Depth (mm)	Wear rate $(10^{-3}$ mm³/min)
1	0.252 ± 0.042	0.583 ± 0.032	2.027 ± 0.622	1.091 ± 2.17	0.078 ± 0.006	0.215 ± 0.038
2	1.188 ± 0.083	0.562 ± 0.025	1.407 ± 0.300	0.71 ± 0.35	0.097 ± 0.014	0.220 ± 0.041
3	1.105 ± 0.161	0.358 ± 0.033	0.913 ± 0.113	0.89 ± 0.031	0.21 ± 0.034	0.236 ± 0.037
4	1.179 ± 0.353	0.302 ± 0.053	1.014 ± 0.182	0.3 ± 0.032	0.194 ± 0.025	0.387 ± 0.040
5	2.362 ± 0.269	0.47 ± 0.016	1.534 ± 0.150	0.472 ± 0.026	0.202 ± 0.038	0.291 ± 0.041

			Room temperature (23°C) wear testing			
Normal force (N)	Initial F_f (N)	Initial COF	Final F_f (N)	Final COF	Depth (mm)	Wear rate $(10^{-6}$ mm³/min)
1	0.047 ± 0.059	0.0619 ± 0.018	0.25 ± 0.099	0.183 ± 0.433	0.0061 ± 0.0008	0.0068 ± 0.0001
2	0.194 ± 0.031	0.101 ± 0.015	0.502 ± 0.064	0.2543 ± 0.032	0.007 ± 0.001	0.0076 ± 0.0001
3	0.417 ± 0.064	0.133 ± 0.021	1.136 ± 0.134	0.386 ± 0.047	0.005 ± 0.001	0.0059 ± 0.0001
4	0.616 ± 0.111	0.147 ± 0.0019	1.664 ± 0.226	0.399 ± 0.046	0.007 ± 0.001	0.0055 ± 0.0001
5	0.825 ± 0.128	0.167 ± 0.026	1.812 ± 0.132	0.368 ± 0.027	0.006 ± 0.001	0.0067 ± 0.0001

not fit other parameters. The initial coefficient of friction was higher at the lower normal loads, but this may be another indication that, with the higher applied load, delamination occurred quickly, almost instantly, and produced a different coefficient of friction.

In the high-temperature tests, one may have expected that the final coefficient of friction values may be equal if the indenter penetrated into the same layer for each test. In fact, the indenter depth indicates that, in all tests, the indenter never penetrated beyond the top coat, so it may seem reasonable to assume that the final coefficient is the coefficient of friction of 8YSZ. However, as shown in Table I, there is a significant variance between the final coefficient of friction values. This variance is likely due to the delamination of the top coat and debris that is carried along the wear track.

At room temperature, several trends were evident. The initial and final friction force and coefficient of friction increased with the applied normal load. While the initial coefficient of friction also seemed to increase with friction, this trend may have been the result of stiction, and the final coefficient of friction was consistent among tests with loads greater than 2 N. Since the indenter did not wear through the top coating, the coefficient of friction should be the same for all tests. While this is consistent at higher normal loads, at loads of 1 N and 2 N, the coefficient was significantly less. With lower applied loads, the indenter likely did not contact enough material due to the uneven topography of the top coat and the final coefficient of friction was therefore reduced.

Figure 3 displays the wear rates at high and room temperature. At room temperature, the rates are consistent, but there is greater variance of wear rates at high temperature. However, the wear rates at a temperature of 1000°C are orders of magnitude greater than at room temperature. These results indicate that temperature is an important parameter in the wear of the thermal barrier coating, more so than the applied load.

Digital Image Correlation

Using optical images of the coating before and after wear, digital image correlation (DIC) was used to identify the extent of wear damage on the surface of the coating using methods as described by Xu et al. in their previous work with DIC.[15] The correlation software identified reference points, undeformed features, between the two images to map the wear and deformed surface features. Figure 4b displays a map overlay on the worn surface of strain in the direction of the oscillating indenter. When DIC could not identify the correlation between the deformed and undeformed, the strain overlay shows no color, indicating a severe degree of surface wear damage, and, as a result, the overlay clearly reveals the wear path in the center of Fig. 4b. All other regions of the coating are shaded to indicate little to no strain. There are small, scattered areas where the correlation fails or indicates some strain, but these regions are likely areas of debris generated during testing. These tests demonstrate that DIC can be used to map the extent of wear and identify regions of severe wear.
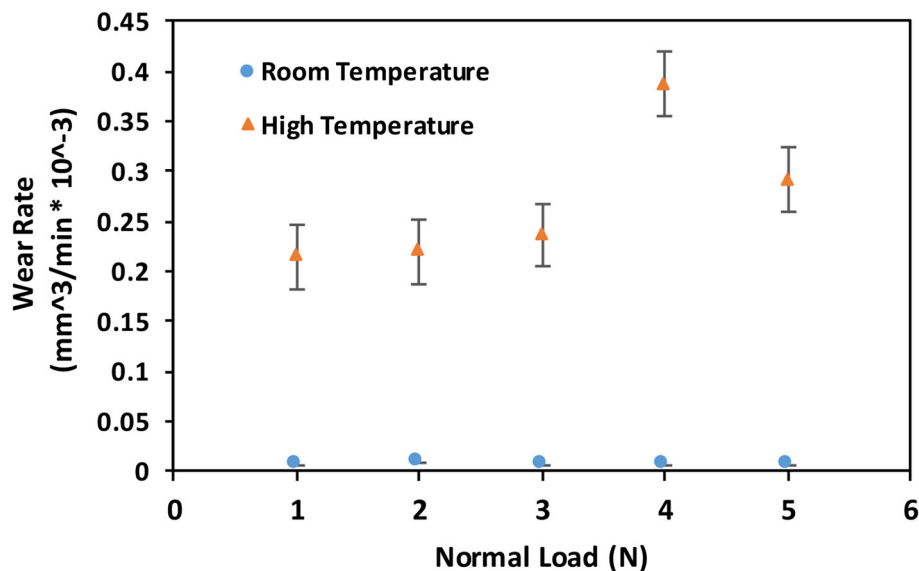
Fig. 3. Graphical representation of obtained wear rates demonstrate significantly higher rates of wear at 1000°C and little variance due to applied normal load.
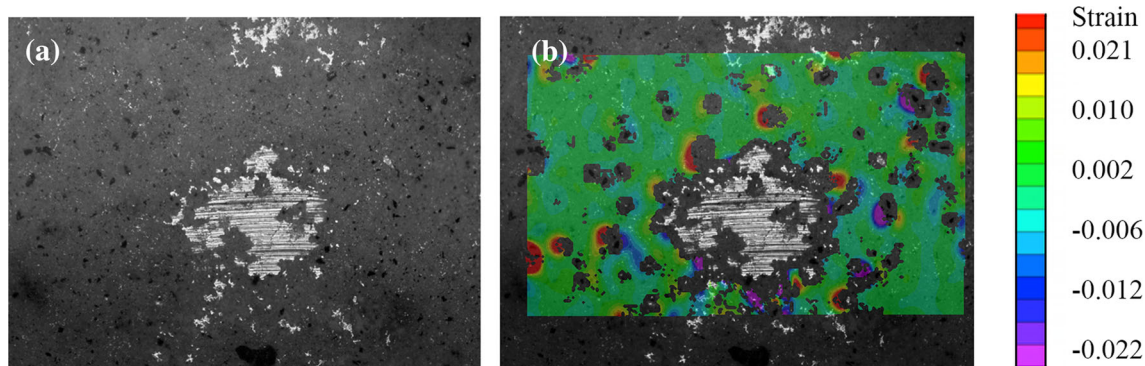

Fig. 4. Digital image correlation between images of the (a) worn coating (5 N load at 23°C) to identify the extent of wear damage to the coating as shown by (b) strain mapping. Areas shaded red or purple indicate greater strain.

Energy Dispersive X-ray Mapping

While analysis of friction during wear indicated that delamination had occurred, the wear paths were imaged by scanning electron microscopy (SEM) and energy dispersive x-ray spectrometry (EDX) mapping to determine the chemical makeup of the wear paths. Figure 5 is a series of EDX maps to demonstrate the composition of the different layers of the un-worn thermal barrier coating. The top coat is clearly distinct, prominently shown by the presence of zirconium in Fig. 5f and the relatively low presence of oxygen, aluminum, iron, and nickel compared to the following layers. However, the bond coat is difficult to identify, except for a slightly greater density of aluminum (Fig. 5c). The substrate is indicated by a high presence of aluminum, iron, and nickel, fitting with its element composition (Fig. 5c, d, and e).

After the wear testing at both high and room temperatures, the thermal barrier coating was again imaged by SEM, and new EDX maps were obtained of the most prominent materials detected on the surface of the wear path. Figure 6a shows the wear path of a test conducted at 1000°C and under an applied load of 3 N taken in the SEM. EDX mapping of zirconium in Fig. 6c shows the wear path clearly visible, indicating that the indenter had almost worn entirely through the top coat while Fig. 6b and d shows an increase of iron and oxygen along the wear path. At 1000°C, the indenter had entirely or had nearly worn through the top coat of zirconia to expose the greater concentration of oxygen and iron in the bond coat and substrate, fitting the wear analysis which found the indenter depth approached the top coat/bond coat interface.

In contrast, Fig. 6e, f, g, and h shows the wear path of a test conducted at room temperature and under an applied load of 3 N. In Fig. 6e, the wear path is faintly visible, but Fig. 6f, g, and h does not display any indication of material wear. Figure 6g shows that the map of zirconium is not affected by the wear, so the indenter did not penetrate the top coat.
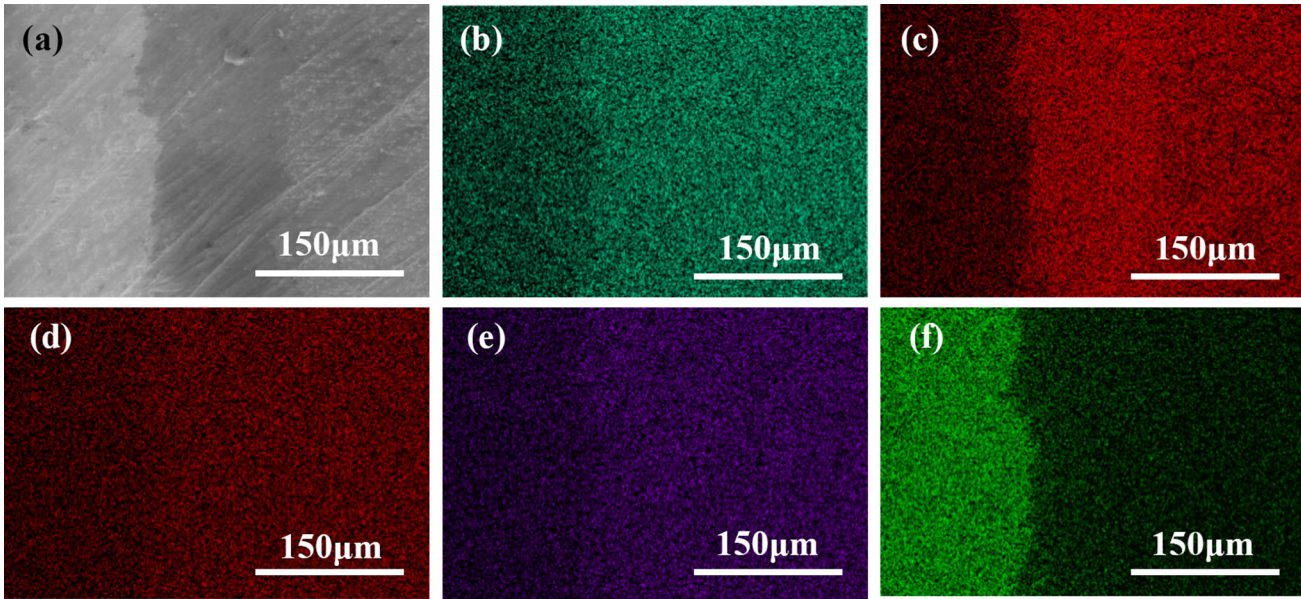
Fig. 5. A cross-sectional view of the thermal barrier coating as an (a) SEM image and as EDX maps of (b) oxygen, (c) aluminum, (d) iron, (e) nickel, and (f) zirconium.

Vickers Indentation Testing

Indentation tests were also conducted on the sample at both room temperature and 1000°C to compare the hardness of the coating layers. A sapphire Vicker's indenter with an included angle of 136° was used for all hardness testing. Figure 7a, b, and c shows the indentations made at room temperature under an applied load of 30 N. Figure 7d, e, and f show the indentations made at 1000°C under an applied load of 15 N. The diagonals of the indentions were measured and used to calculate the hardness. The Vickers hardness values, HV, is found using the equation:

$$\text{HV} = \frac{F}{A} = \frac{F}{(d_1 d_2)/(2 \sin(\theta))} \quad (1)$$

where θ of 68° is half the indentation angle, and d_1 and d_2 are the diagonals of the indentation.[16] The hardness values are listed in Table II.

From Table II, it is clear that the top coat is the hardest layer followed by the bond coat at both temperature conditions. However, temperature has a significant impact on the coating hardness. The top coat hardness value decreases by 41%, even though it still remains the hardest layer at 1000°C. The softening of the thermal barrier coating at elevated temperatures may be a contributing factor to the delamination that occurs.

The hardness values obtained at room temperature agree with prior work. The hardness of 8YSZ is difficult to narrow down, but the value of 593 HV, which converts to a 5.6 GPa hardness value, fits neatly within the range of 3.5–5.8 GPa specifically reported by Jang et al. and Kwon et al.[16–18]

Hertz Contact Modeling and Finite Element Analysis

Having measured friction and examining the wear paths under the microscope, there appears to be delamination occurring in all high-temperature wear testing and no delamination at room temperature. Exactly why this delamination occurs in this pattern may be revealed through a comparison of an impact model and the physical data.

A Hertzian contact model provides a fundamental understanding of the contact between two elastic bodies. The theory assumes the interaction is frictionless, hence the only interaction is the applied normal load. In this case, one body is a sphere, the alumina indenter with a radius of 3.15 mm as shown in Fig. 8. The other body is the thermal barrier coating, which, as a flat plane, has a radius of curvature going to infinity.[14]

Using a Hertz contact model, it is possible to calculate the maximum shear and its depth below the contact area. First, the maximum pressure, $P_{\max}$, is determined using the equation:

$$P_{\max} = \frac{3F}{2\pi a^2} \quad (2)$$

where a is the contact radius and F is the applied force. The contact radius is found as follows:

$$a = \sqrt[3]{\frac{3F}{8} \frac{(1-v_1^2)/E_1 + (1-v_2^2)/E_2}{\frac{1}{d_1} + \frac{1}{d_2}}}. \quad (3)$$

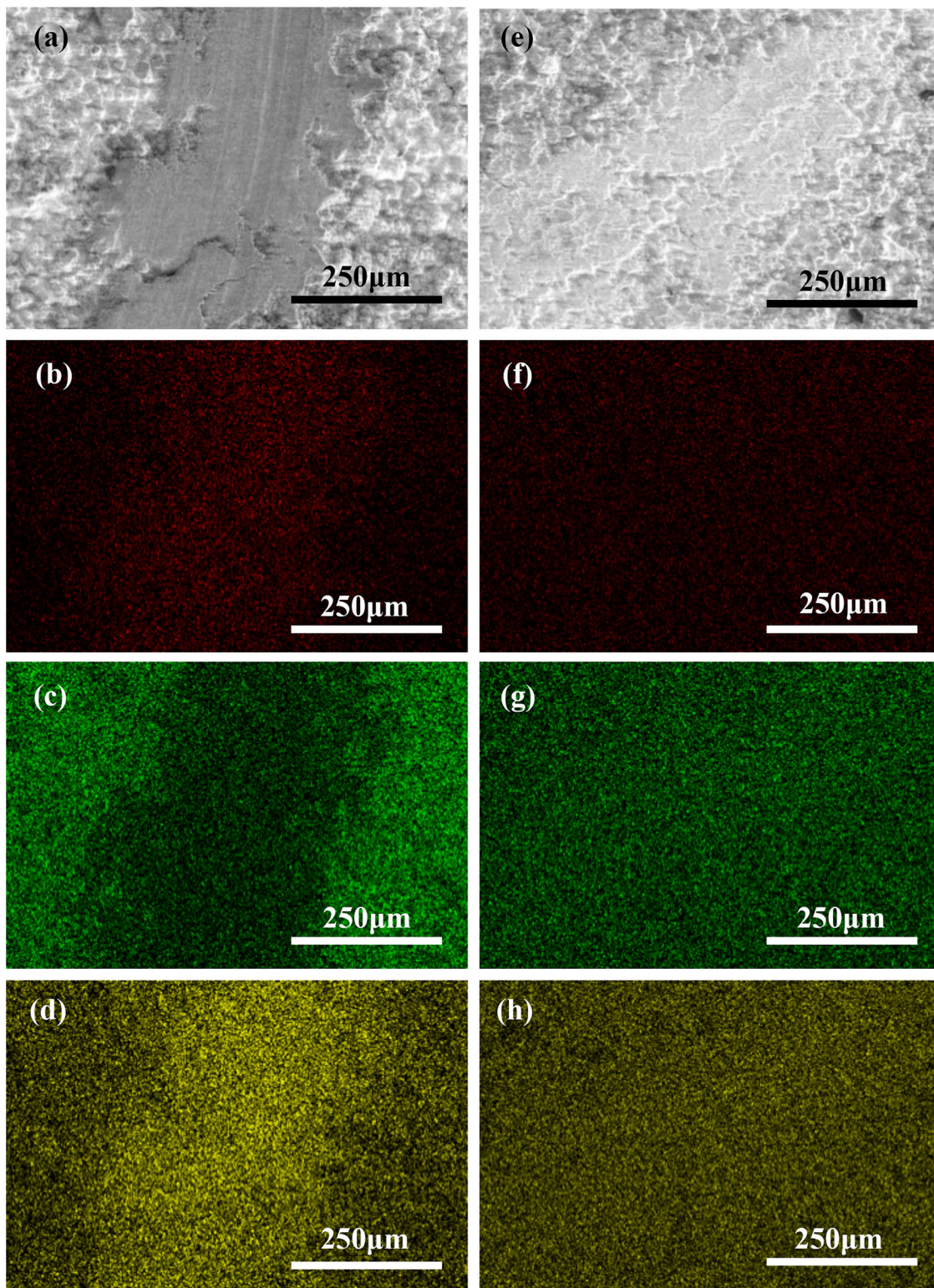The maximum shear stress, $\tau_{\max}$, is determined with the simple equation:

Fig. 6. The wear track under a load of 3 N at 1000°C was imaged under and SEM subjected to EDX mapping, yielding (a) SEM image of the wear, (b) a map of iron, (c) a map of zirconium, and (d) a map of oxygen. The corresponding wear track under a load of 3 N at room temperature are shown as (e) a SEM image of the wear, (f) a map of iron, (g) a map of zirconia, and (h) a map of oxygen.
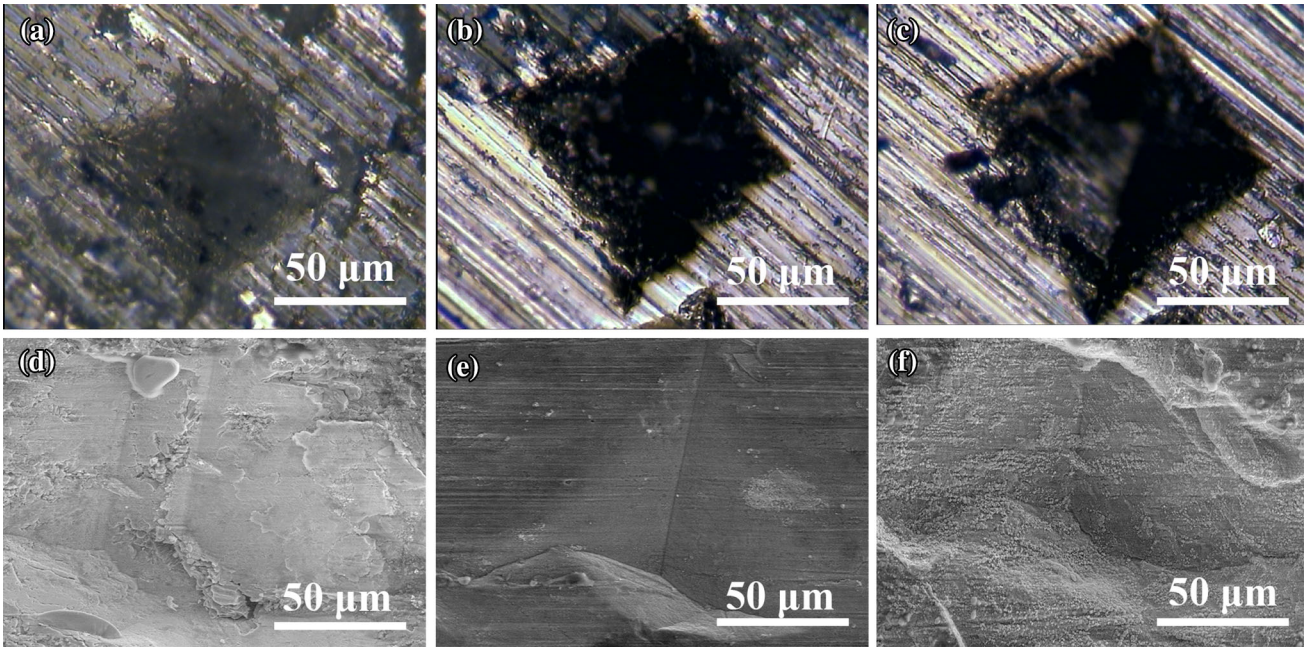
Fig. 7. Optical images of Vickers indentation testing preformed at room temperature under an applied load of 30 N. The indentations were made in the (a) top coat, (b) bond coat, and the (c) Ni alloy substrate, and SEM images of Vickers indentation testing preformed at 1000°C and under an applied load of 15 N. The indentations were made in the (d) top coat, (e) bond coat, and the (f) Ni alloy substrate.

Table II. The hardness values of the coating layers from Vickers indentation testing and room temperature and 1000°C

Material	HV at 23°C	HV at 1000°C	Percent diff. (%)
Top coat (8YSZ)	593 ± 14	352 ± 16	−41
Bond coat (NiCoCrAlY)	397 ± 11	251 ± 13	−37
Substrate (Ni superalloy)	249 ± 8	220 ± 9	−12

$$\tau_{\max} = \frac{\sigma_x - \sigma_z}{2} \qquad (4)$$

where σ_x and σ_z represent the principal stresses. The principal stresses are determined as follows:[14]

$$\sigma_x = -P_{\max}\left[\left(1 - \left|\frac{z}{a}\right|\right)\tan^{-1}\left(\frac{1}{\left|\frac{z}{a}\right|}\right)(1+v) - \frac{1}{2\left(1+\frac{z^2}{a^2}\right)}\right] \qquad (5)$$

$$\sigma_z = \frac{-P_{\max}}{1 + \frac{z^2}{a^2}} \qquad (6)$$

The Young's modulus and Poisson's ratio of the indenter and thermal barrier coating are presented in Table III. The calculated shear and depth are listed in Table IV. The "depth to max shear" column was tabulated by combining the indenter depth from Table I with the relative depth from the point of contact. Using this total depth to the maximum shear, it is possible to identify the region or layer.
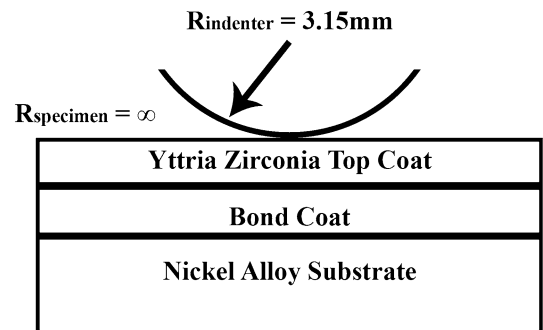

Fig. 8. A Hertzian contact model of the interaction between a spherical indenter and flat barrier coating.

As shown in Table IV, the maximum shear stress during wear occurred deeper in the coating as the applied normal load increased for both temperature conditions. However, at room temperature, the maximum shear occurred only within the top coat. In contrast, at high temperature, the shear stress occurred deeper within the coating than it did at

room temperature, moving into the interface region between the top coat and bond coat at normal loads greater than 2 N.

These results were corroborated by a simple finite element model (FEM) of a Hertzian indentation. Finite element models are frequently used to better understand the stresses present under different loading conditions, coating materials, and temperatures. Previously, Diao et al. developed a finite element model to evaluate sliding contact on a hard coating in order to evaluate the maximum shearing stresses and the effect of coating thickness and friction, determining that a hard interlayer reduced the internal stresses during contact.[7] Similarly, Ahmadian et al. used an FEM analysis to determine that parallel cracking within the top coat prompted coating failure.[19] Building from the success of prior FEM analysis, the contact with the data presented in Table I, a similar finite element approach was

applied using the material properties of the specific coating at both room and high temperatures. Using LS-DYNA, the thermal barrier coating layers were modeled and subjected to a vertical indentation and lateral oscillations matching the behavior in the physical system during the high temperature tests. Figure 9a shows the shear stress distribution of the top coat layer and clearly reveals that the maximum shear stress does not occur until the interface with the bond coat. Additionally, the finite element model reveals a ring of higher stress outside the contact area as shown in Fig. 9b.

Furthermore, the values of maximum shear stress decreased for the high temperature testing, yet delamination occurred only at higher temperature. The depth of the stress played a larger role in the coating failure than the magnitude of the shear stress. From this Hertz contact model, it is apparent the maximum shear stress occurred at or near to the interface between the top and bond coatings at 1000°C. This interface may then be the area of delamination indicated by the frictional analysis. Delamination and separation at this interface may also account for the increase in inelastic strain observed by Ahmadian et al. at higher temperatures.[19]

Recent studies of the thermal properties of thermal barrier coatings have identified the thermal expansion coefficient (TEC) of the each of the different coating layers used this particular specimen, as listed in Table V.[23,24] From these coefficient values, the thermal stress experienced by each layer was also calculated using the equation:

$$\sigma_T = \text{TEC} * E * \Delta T, \tag{7}$$

Table III. The Young's modulus and Poisson's ratio for alumina and 8YSZ, the thermal barrier coating as determined in previous studies[20–22]

	Alumina indenter	8YSZ top coat
23°C		
Young's modulus (GPA)	375	53
Poisson's ratio	0.24	0.31
1000°C		
Young's modulus (GPA)	331	46
Poisson's ratio	0.21	0.27

Table IV. The calculated maximum shear stress and its depth beyond the contact point with the indenter

		Room temperature contact model analysis			
Normal load (N)	Indenter depth (mm)	Max shear (MPa)	Relative depth to max shear (μm)	Depth of max shear (μm)	Region of max shear
1	0.0061 ± 0.0008	114.9	17.22	23.32 ± 0.84	Top coat
2	0.007 ± 0.001	144.7	21.7	28.7 ± 0.9	
3	0.005 ± 0.001	165.7	24.84	29.84 ± 0.9	
4	0.007 ± 0.001	182.4	27.34	34.34 ± 1.4	
5	0.006 ± 0.001	196.4	29.45	35.45 ± 0.9	

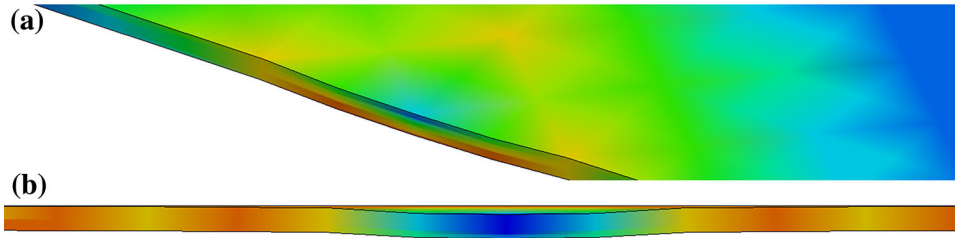|		High temperature contact model analysis			
Normal force (N)	Indenter depth (mm)	Max shear (MPa)	Relative depth to max shear (μm)	Total depth of max shear (μm)	Region of max shear
1	0.078 ± 0.006	103.1	18.17	96.17 ± 5.9	Top coat
2	0.097 ± 0.014	130	22.9	119.9 ± 14.1	
3	0.21 ± 0.034	148.8	26.21	236.21 ± 33.7	Top coat/bond coat interface
4	0.194 ± 0.025	163.8	28.85	222.85 ± 24.7	
5	0.202 ± 0.038	176.4	31.08	233.08 ± 38.4	

Fig. 9. Finite element models of (a) a top and cross-sectional view of the shear stress distribution of the top coat, showing the maximum shear stress at the interface with the bond coat and of (b) a cross-sectional view of the z-stress (orthogonal to the surface of the coating) distribution through the top coat of the thermal barrier coating, showing an outer ring of high stress.

Table V. The thermal expansion coefficients of each layer within the specimen as identified in previous studies[23,24]

Material	TEC ($*10^{-6}$/°C)	Thermal stress (GPa)
Top coat (8YSZ)	12	0.55
Bond coat (NiCoCrAlY)	17.9	3.56
Substrate (Ni superalloy)	18	2.18

where σ_T is the thermal stress, E is the Young's modulus, and ΔT is the thermal gradient.[24] The difference between the expansion coefficient and thermal stress of the top coat and the remaining two coatings is readily apparent. The bond coat and the nickel alloy substrate have coefficient values that are nearly the same, meaning that, as the specimen heats up, they will expand similarly. However, the top coat has a lower coefficient and a lower thermal stress and will not expand as much as the bond coat beneath it. As a consequence of the significant difference in thermal stress and expansion at high temperature along this top coat/bond coat interface, this region is the likely location of delamination. Zhao et al. have demonstrated how varying rates of thermal expansion among coating layers can lead to spallation or delamination, indicating that thermal expansion may be the underlying cause of the coating failure in this research as well.[25]

Stress and Fracture Energy

The SEM images of cracking and delamination confirm the Hertz contact model analysis that only the top coat failed. With this knowledge, the fracture energy (G) was calculated from the maximum shear stress ($\tau_{\max}$) using the equation:

$$G = \tau_{\max} * d/2 \qquad (8)$$

The value d is the separation of the coating. The stress intensity factor (K) was also calculated:[26,27]

$$K = \left(\frac{EG}{1 - v^2}\right)^{1/2} \qquad (9)$$

The fracture energy and stress intensity factors of the five loading scenarios during the high temperature tests at 1000°C are listed in Table VI.

In a previous study, Xu et al. were able to correlate the nominal shear stress to interfacial properties, fracture energy and stress intensity factor. The fracture energy and stress intensity factors calculated in Table VI fit with the range determined in this study, reading an ultimate shear stress corresponding to a fracture energy of about 450 J/m².[27] The calculated values in Table VI follow a progression of increasing maximum shear stress combined with an interfacial thermal stress gradient to an ultimate shear stress with corresponding increases in the fracture energy and stress intensity factor to a maximum.

Previous studies have focused solely on thermal expansion, contact stresses, or coating material properties to identify the factors contributing to coating failure. However, from the analysis presented, it is clear that there are two critical factors for failure and delamination—a thermal stress disparity between coating layers and the depth of maximum shear stress. From the lack of visible cracking or delamination and the frictional analysis, it can be concluded that interfacial bond between the coating layers is stronger than the applied shear stress during wear at room temperature even though the maximum shear stresses are slightly higher at 23°C than those at 1000°C. However, as indicated in the SEM images, frictional analysis, and Hertz contact model, the depth of the maximum shear stress and the presence of a thermal stress disparity overcame the interfacial bonds of the top coat/bond coat interface, leading to delamination.

Imaging Delamination

Having used frictional analysis and a Hertz contact model to identify delamination at the top coat/bond coat interface as the mechanism of failure of the thermal barrier coating, SEM images were obtained of cross-sectional cuts of wear paths on the specimen to verify the conclusions. Figure 10 presents images of the wear damage when the indenter oscillates in a direction corresponding

Table VI. Fracture energy and stress intensity factor calculated with the corresponding maximum shear stress during the high temperature (1000°C) testing

Applied load (N)	Max shear stress (MPa)	Fracture energy (J/m^2)	Stress intensity factor (MPa/m^2)
1	103.1	258	3.52
2	130.0	325	3.96
3	148.8	372	4.23
4	163.8	410	4.44
5	176.4	441	4.61

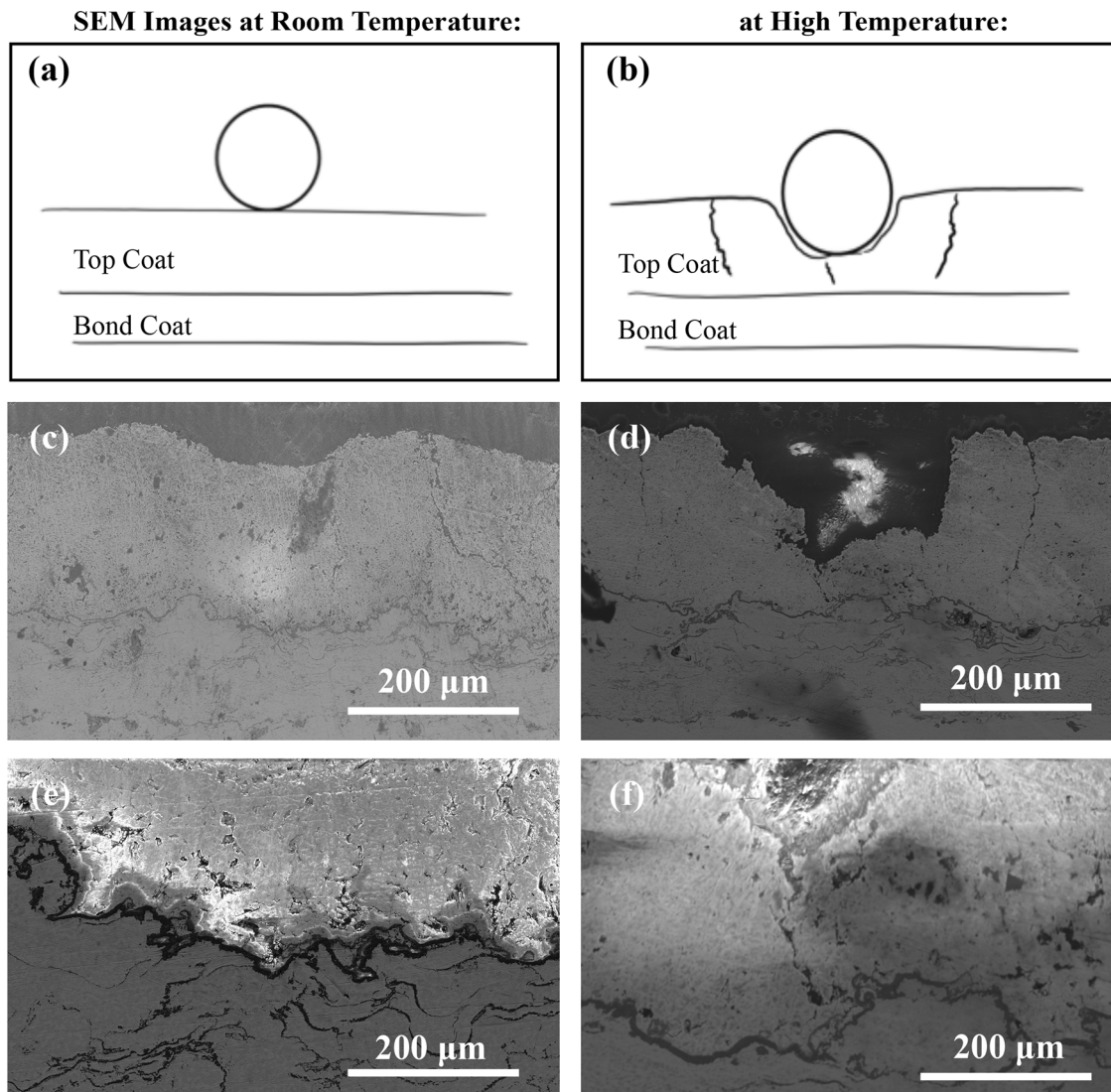**SEM Images at Room Temperature:**   **at High Temperature:**

Fig. 10. Cross-sectional cuts of the specimen were made to show internal wear damage such that the direction of the indenter oscillations were back and forth orthogonal to the picture plane and imaged using a SEM. The images show a depiction of the thermal coating after wear at (a) room temperature and (b) high temperature, SEM images of the coating at (c) room temperature and (d) high temperature, and higher magnification SEM images of the top coat/bond coat interface at (e) room temperature and (f) high temperature.

perpendicular to the page. As expected, there were no signs of cracking or delamination in unworn areas nor in areas worn at room temperature (Fig. 10a, c, and e). However, Fig. 10c does clearly

show the depression made from the indenter. Figure 10e, which shows the top coat/bond coat interface at higher magnification, does not show any added cracking or delamination.
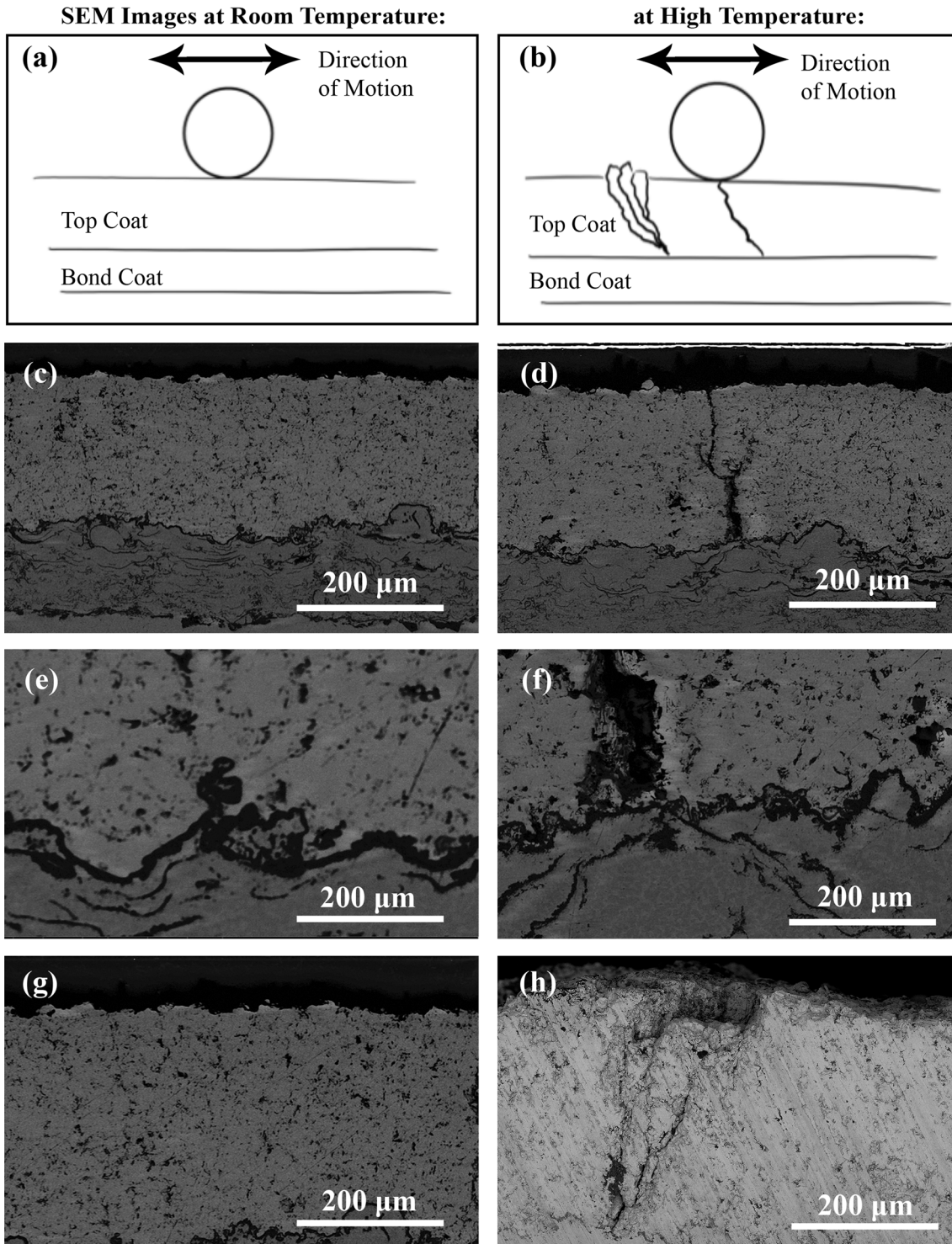
Fig. 11. Cross-sectional cuts of the specimen were made to show internal wear damage such that the direction of motion were from side to side, parallel with the picture plane and imaged using a SEM. The images show a depiction of the thermal coating after wear at (a) room temperature and (b) high temperature, SEM images of the coating at (c) room temperature and (d) high temperature, and higher magnification SEM images of the top coat/bond coat interface at (e) room temperature and (f) high temperature.

In contrast, there is significant cracking and damage at high temperature (Fig. 10b, d, and f). Figure 10d clearly shows the deep wear depression left by the indenter as well as two lateral cracks running through the top coat layer. These lateral cracks are likely caused by the outer ring of higher stress revealed by the finite element model in Fig. 9. Figure 10f also shows cracking extending from the

bottom of the wear track to the bond coat. The cracking stops at the interface, indicating delamination of the top coat only.

Figure 11 depicts another cross-section cut made such that the direction of the indenter was from side to side. As before, Fig. 11a, c, e, and g reveal that there is no additional cracking or damage during the room temperature tests. However, Fig. 11b, d, and f depict a large crack, representative of the type of cracking found in the top coat during high temperature tests. These cracks occurred as the indenter moved from side to side, pushing and pulling on the top coat, causing it to tear apart in some places (Fig. 11d) or collapse and buckle in others (Fig. 11h). As shown in Fig. 11d, f, and h, the cracks and buckling are observed to traverse the top coat to the bond coat interface. These SEM images (Figs. 10 and 11) confirm the finding that only the top coat failed at high temperatures and due to delamination. These images further support the conclusion of the effects of shear and thermal stress combining to achieve the fracture energy at the depth of the top coat/bond coat interface.

CONCLUSION

Delamination of thermal barrier coatings at high temperatures is the likely cause of coating failure. Using frictional analysis of the wear preformed on a sample of thermal barrier coating, it is possible to identify the point of delamination. Optical and SEM imaging and EDX mapping are able to identify the extent of wear damage. Furthermore, a Hertz contact model can be used to readily analyze the data gathered in tribological testing to locate the depth of maximum shear stress within the coating layers. However, the crucial factor in delamination is the presence of a significant thermal stress difference between the coating layers. Other factors such as contact stresses and friction do not contribute significantly to coating failure. From this comprehensive analysis, it is clear that delamination occurs between the top coat and bond coat due to the maximum shear stresses, occurring at the right depth between the coating layers and where there is a critical thermal stress disparity, to achieve the necessary fracture energy.

REFERENCES

1. R.K. Mishra and C.J. Beura, *Fail. Anal. Prevent.* 14, 519–529 (2014).
2. C. Meher-Homji and G. Gabriles, Gas turbine blade failures—causes, avoidance, and troubleshooting. *Proceedings of the 27th Turbomachinery Symposium*, pp. 129–179.
3. C. Lamuta, G.D. Girolamo, and L. Pagnotta, *Ceram. Int.* 41, 8904–8914 (2015).
4. L. Su, W. Zhang, X. Chen, and T.J. Wang, *Ceram. Int.* 41, 8945–8955 (2015).
5. Y. Han, F. Ye, K. Ding, Z. Wang, and G. Lu, *Trans. Nonferrous Met. Soc. China* 22, 1629–1637 (2012).
6. R.T. Wu, X. Wang, and A. Atkinson, *Acta Mater.* 58, 5578–5585 (2010).
7. D.F. Diao, Y. Sawaki, and H. Suzuki, *Surf. Coat. Technol.* 86–87, 480–485 (1996).
8. A. Moridi, M. Azadi, and G.H. Farrahi, *Surf. Coat. Technol.* 243, 91–99 (2014).
9. Z. Chen, M.Y. He, I. Spitsberg, N.A. Fleck, J.W. Hutchinson, and A.G. Evans, *Wear* 256, 735–746 (2004).
10. L. Yang, F. Yang, Y. Long, Y. Zhao, X. Xiong, X. Zhao, and P. Xiao, *Surf. Coat. Technol.* 251, 98–105 (2014).
11. V.P. Deodeshmukh, S.J. Matthews, and D.L. Klarstrom, *Int. J. Hydrogen Energy* 36, 4580–4587 (2011).
12. J.Y. Tong, X.F. Ding, M.L. Wang, Y.R. Zheng, K. Yagi, and Q. Feng, *Mater. Sci. Eng., A* 618, 605–613 (2014).
13. F. Sun, J. Tong, Q. Feng, and J. Zhang, *J. Alloy. Compd.* 618, 728–733 (2015).
14. K. L. Johnson, *Contact Mechanics.* (1987).
15. Z.H. Xu, M.A. Sutton, and X.D. Li, *Acta Mater.* 56, 6304–6309 (2008).
16. S. Nath, I. Manna, and J.D. Majumdar, *Ceram. Int.* 41, 5247–5257 (2015).
17. H. Jang, Y. Park, J. Jung, J. Jang, S. Choi, and U. Paik, *Surf. Coat. Technol.* 200, 4355–4362 (2006).
18. J.Y. Kwon, J.H. Lee, H.C. Kim, Y.G. Jung, U. Paik, and K.S. Lee, *Mater. Sci. Eng., A* 429, 173–180 (2006).
19. S. Ahmadian, C. Thistle, and E. Jordan, *J. Am. Ceram. Soc.* 96, 3210–3217 (2013).
20. P. Auerkari, *VTT Manufacturing Technology* 1–26 (1996).
21. W. Pabst, E. Gregorova, and M.J. Cerny, *Eur. Ceram. Soc.* 33, 2085–3093 (2013).
22. J.M. Antunes, J.V. Fernandes, N.A. Sakharova, M.C. Oliveira, and L.F. Menezes, *Int. J. Solids Struct.* 44, 8313–8334 (2007).
23. R. Tu and T. Goto, *Mater. Trans.* 46, 1318–1323 (2005).
24. Y. Song, Z. Lv, Y. Liu, X. Zhuan, and T.J. Wang, *Appl. Surf. Sci.* 324, 627–633 (2015).
25. S. Zhao, Y. Zhao, B. Zou, X. Fan, J. Xu, Y. Hui, X. Zhou, S. Liu, and X. Cao, *J. Alloys Compd.* 592, 109–114 (2014).
26. T. Diehl, *Int. J. Adhes. Adhes.* 28, 2237–2255 (2008).
27. Z.H. Xu, Y.C. Yang, P. Huang, and X.D. Li, *Acta Mater.* 58, 5972–5979 (2010).